

# Surrogate Modeling of Ultrasonic Nondestructive Evaluation Simulations

Jacob Siegler<sup>1</sup>, Leifur Leifsson<sup>1,2</sup>, Robert Grandin<sup>1</sup>, Slawomir Koziel<sup>2</sup>, and  
Adrian Bekasiewicz<sup>2</sup>

<sup>1</sup>*Iowa State University, Ames, Iowa, USA<sup>\*,†</sup>*

<sup>2</sup>*Reykjavik University, Reykjavik, Iceland<sup>‡</sup>*

*jsiegler@iastate.edu, leifur@iastate.edu, rgrandin@iastate.edu, koziel@ru.is, bekasiewicz@ru.is*

## Abstract

Ultrasonic testing (UT) is used to detect internal flaws in materials or to characterize material properties. Computational simulations are an important part of the UT process. Fast models are essential for UT applications such as inverse design or model-assisted probability of detection. This paper presents investigations of using surrogate modeling techniques to create fast approximate models of UT simulator responses. In particular, we propose to use data-driven surrogate modeling techniques (kriging interpolation), and physics-based surrogate modeling techniques (space mapping), as well a mixture of the two approaches. These techniques are investigated for two cases involving UT simulations of metal components immersed in a water bath during the inspection process.

**Keywords:** Nondestructive evaluation, ultrasonic testing, inverse design, model-assisted probability of detection, surrogate modeling, kriging interpolation, space mapping, mixed modeling.

## 1 Introduction

Techniques for analyzing material, components, or systems without causing damage are referred to as nondestructive evaluations (NDE). Ultrasonic testing (UT) is a specific family of NDE techniques which are based on the propagation of high-frequency stress waves in the object or material under examination (Thompson and Gray, 1983; Roberts, 2004). Common UT applications involve very short ultrasonic pulse-waves being transmitted into materials to detect internal flaws or to characterize material properties. Computational models can play an important role in the UT process, such as in inverse design where the models are used to identify parameters of flaws using experimental results as the a priori data (Berens, 1989). The UT models are also used to evaluate the probability of detecting (POD) flaws, so-called model-assisted POD (MAPOD) (Smith *et al.*, 2007; Meeker, 2012; Thompson *et al.*, 2012). The UT inspection can be simulated using models of varying fidelity, such as those based on the Asymptotic Green's Function (Roberts, 2004) or Gaussian-Hermite Series Expansions (Thompson and Gray, 1983).

<sup>\*</sup> Department of Aerospace Engineering, 2271 Howe Hall, Ames, IA 50011, USA.

<sup>†</sup> Center for Nondestructive Evaluation, 1915 Scholl Road, 111 ASC II, Ames, IA 50011, USA.

<sup>‡</sup> Engineering Optimization & Modeling Center, School of Science and Eng., Menntavegur 1, 101 Reykjavik, Iceland.

Although the computational cost of a single simulation may not be very high (often on the order of minutes), it can be prohibitive to use such models directly for inverse design or MAPOD analyses due to a large number of required evaluations.

Surrogate models are widely used to create fast approximate models ((Queipo *et al.*, 2005; Forrester and Keane, 2009; Koziel *et al.*, 2011). Surrogate modeling approaches can be roughly divided into two categories: (i) data-driven (or approximation-based) and (ii) physics-based. Data-driven surrogate models are constructed through approximations of the high-fidelity model data obtained in the process of sampling the design space using appropriate design of experiments (DOE) methodologies (Queipo *et al.*, 2005; Forrester and Keane, 2009). Data-driven surrogates can be considered as generic models that are independent of the physics or any other knowledge about the problem at hand. The other class of models is based on exploitation of some knowledge about the system under consideration, usually embedded in physics-based low-fidelity models (Koziel *et al.*, 2011).

In this paper, we investigate the use of surrogate modeling techniques to create fast approximate models of UT simulator responses. In particular, we apply kriging interpolation (Journel and Huijbregts, 1981; Simpson *et al.*, 2001; Kleijnen, 2009), multi-point space mapping (Bandler *et al.*, 2004), and a combination of the two (Koziel and Bandler, 2012) to the modeling of UT simulations of metal components immersed in a water bath. The paper is organized as follows. The basics of the UT NDE process and the UT simulation models are described in Section 2. In Section 3, we give the details of surrogate modeling techniques used in this work. Section 4 presents the results of numerical examples. Section 5 concludes the paper.

## 2 Ultrasonic Nondestructive Evaluation Simulations

This section describes, in general, ultrasonic nondestructive evaluations, and gives an outline of two widely used simulation approaches for ultrasonic testing.

### 2.1 Ultrasonic NDE and Model-Assisted POD

Techniques for analyzing materials, components, or systems without inducing damage during are called nondestructive evaluation (NDE). NDE is commonly performed using many inspection modalities, including electromagnetic fields, x-ray radiation, and ultrasonic acoustic energy. Ultrasonic testing (UT) is very commonly used due to its lack of adverse health concerns, unlike x-ray radiation, and ability to penetrate beyond the surface of the inspected component, unlike most electromagnetic techniques (Thompson and Gray, 1983; Roberts, 2004). UT equipment is also quite portable, making it well-suited for use in the field and on the flight line. In a typical UT inspection ultrasonic acoustic energy, often of megahertz frequency, is generated by a piezoelectric transducer. This energy impinges on the specimen being inspected and a portion of the energy is transmitted through the surface. The transmitted energy interacts with the specimen material, as well as any internal structures and defects, generating echoes which are reflected back towards the transducer. These echoes transmit back through the specimen surface and are measured by the piezoelectric transducer. The measurement signal is a waveform depicting the echo amplitude as a function of time. Most-commonly, the key metric of the inspection is the maximum amplitude of the measured waveform, as larger echoes are caused by larger internal reflectors such as cracks and other defects. A typical setup is shown in Fig. 1.

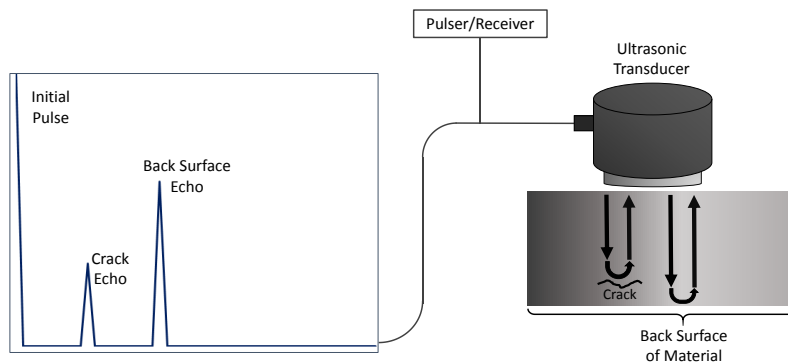


**Figure 1:** Sketch of a typical UT inspection setup. Acoustic energy is generated by the ultrasonic transducer, and is then reflected off both the internal crack and the back wall of the sample. The echo is measured by the transducer and signal amplitude as a function of time is plotted on the data acquisition display. Notice that the crack echo appears earlier in time than the back surface echo due to the shorter round-trip distance traversed by the ultrasonic pulse when it interacts with the internal crack.

When performing any NDE inspection it is essential to have confidence that the obtained measurement is meaningful. For example, if one is concerned about the presence of fatigue cracks in metal, one must have confidence that the chosen inspection is suitably sensitive to such defects (Berens, 1989). This confidence is quantified by calculating the probability of detection (POD) (Smith et al., 2007; Meeker, 2012). In its simplest form, POD can be thought of as the likelihood that an inspector will find a given-size flaw during an inspection. In practice, POD is quite complicated due to the many sources of variability, such as defect orientation, variation of material properties, variation of equipment, and operator-to-operator variability. Obtaining a POD curve which relates flaw size to its likelihood of detection is an expensive process due to both the significant man-hours required by the test inspectors and the resources required to generate the necessary assortment of carefully-fabricated test samples containing known flaws (MIL-HDBK-1823A, 2009). The typical form of a POD curve is shown in Fig. 2.

## 2.2 Gaussian Hermite Series Expansion

The Gaussian-Hermite beam model is a computationally efficient approach which utilizes the Fresnel-approximation. This beam model is implemented using Thompson-Gray measurement model (Thompson and Gray, 1983) and has been a standard method of simulating ultrasonic inspections for over 30 years. Due to its computational efficiency, the Gaussian-Hermite model has several important constraints which do not pose a burden for the majority of inspection scenarios. However, it is often the case that POD simulations and measurements are desired for troublesome geometry and the constraints of the Gaussian-Hermite model become important. These constraints include limited accuracy at highly-oblique incidence and the inability to handle a non-uniform specimen surface within the footprint of the ultrasonic beam. In cases where these constraints are violated, it may be possible to apply post-simulation corrections to leverage the computational efficiency while minimizing the model error.

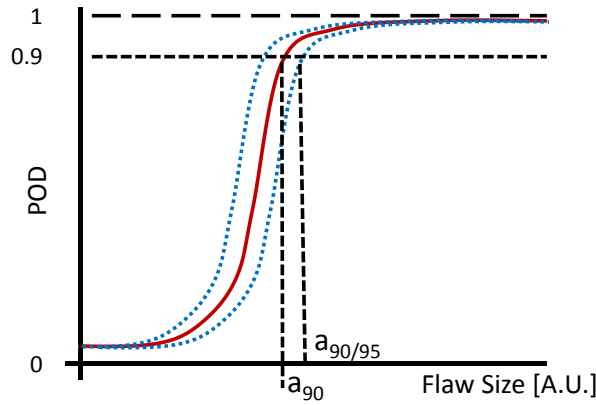


**Figure 2:** The typical form of a POD curve, with the nominal probability of detection given by the red line (Thompson *et al.*, 2012). For small flaw sizes the POD is very small, but non-zero due to noise and measurement error. As the flaw size increases so does the likelihood of detecting the flaw during the NDE inspection, approaching a probability of 1 for large flaw sizes. Just as measurement noise and error can cause missed calls for small flaws, the same types of error prevent the POD from becoming unity even for very large flaws. Also included on POD curves are 95% confidence bounds. It is important to remember that POD is an *estimate* of a statistical random variable and the certainty of that estimate must be quantified. In many cases, the final product of a POD curve is the flaw size,  $a$ , for which there is a 90% likelihood of detection. This flaw size is noted  $a_{90}$ . Being a statistical estimate, one often uses the  $a_{90}$  value which corresponds to the 95% confidence bound, noted as  $a_{90/95}$ . The  $a_{90/95}$  value represents the flaw size for which there exists a 95% confidence that the given-size flaw will be detected 90% of the time.

### 2.3 Asymptotic Green's Function

A less-efficient beam model is based on the evaluation of an asymptotic Green's function. This approach considers a more explicit characterization of both the UT transducer and specimen surface geometry, which allows it to overcome the limitations of the Gaussian-Hermite model (Roberts, 2004). The AGF approach has its own constraints, however, including the increased computational cost and “tuning” required for each specific inspection. When the AGF approach has been required by the modeling scenario, though, it has been shown to provide excellent results (Roberts and Friedl, 2005; Roberts *et al.*, 2011).

## 3 Surrogate Modeling

In this section, we formulate the surrogate modeling problem and describe a few modeling approaches. In particular, we describe data-driven surrogates modeling using kriging interpolation, physics-based modeling using space mapping, and mixed modeling.

### 3.1 Formulation of the Modeling Problem

Let  $\mathbf{f}: X_f \rightarrow R^m$ ,  $X_f \subseteq R^n$  denote the high-fidelity model response vector of the structure of interest. The task is to build a surrogate model  $\mathbf{s}$  of  $\mathbf{f}$  so that the match between the two models is as good as possible in the region of interest  $X_R \subseteq X_f$ . Typically,  $X_R$  is an  $n$ -dimensional interval in  $R^n$  with center at the reference point  $\mathbf{x}^0 = [x_{0,1} \dots x_{0,n}]^T \in R^n$  and size  $\delta = [\delta_1 \dots \delta_n]$ . The quality of the surrogate can be assessed using a suitable error measure, for example, the relative error measure  $\|\mathbf{f}(\mathbf{x}) - \mathbf{s}(\mathbf{x})\|/\|\mathbf{f}(\mathbf{x})\|$  expressed in percent, where  $\mathbf{f}(\mathbf{x})$  and  $\mathbf{s}(\mathbf{x})$  denote the high-fidelity and the respective surrogate model

response at a given test point (design)  $\mathbf{x}$ . The figures of merit are the average and maximum errors over a set of test points. Typically, the test points are allocated in  $X_R$  using a uniform space filling design of experiments such as Latin Hypercube Sampling (LHS) (Forrester and Keane, 2009).

### 3.2 Approaches to Surrogate Modeling

Data-driven surrogates are constructed from the sampled high-fidelity model data (Queipo *et al.*, 2005; Forrester and Keane, 2009). Figure 3 shows the modeling flowchart for this type of models. The first stage is design of experiments (DOE), which is essentially a strategy of allocating required number of samples in the design space. In many cases, the number of training samples is restricted by available computational budget (in certain situations, only a few points may be allowed). Having acquired high-fidelity model data, the model identification is performed using a selected approximation method. The surrogate has to be verified to ensure sufficient accuracy, particularly its generalization capability, i.e., the quality of model predictions at the designs not seen during the identification stage. For that reason, model testing is normally performed using a separate set of testing samples. In practice, the modeling process may be iterative with the flow depicted in Fig. 3 constituting a single iteration.

The main idea behind physics-based surrogates is the exploitation of the knowledge about the system of interest embedded in an underlying low-fidelity (or coarse) model. The latter is a simplified representation of the system (Bandler *et al.*, 2004; Koziel *et al.*, 2011). It is computationally cheaper but, at the same time, less accurate than the high-fidelity model. The low-fidelity model can be obtained, for example, from the same simulator as the one used for the high-fidelity model but using a coarse discretization. Alternatively, the coarse model can be based on simplified physics (e.g., by exploiting simplified equations, or by neglecting certain second-order effects), or on a significantly different physical description (e.g., lumped parameter versus partial differential equation based models). In some cases, coarse models can be formulated using analytical or semi-empirical formulas. Because of its limited accuracy, the low-fidelity model has to be corrected to create a reliable surrogate. The main advantage of physics-based models is that—because of exploiting some knowledge embedded in the low-fidelity model—a limited amount of high-fidelity data is necessary to ensure decent accuracy. For the same reason, physics-based surrogates are characterized by good generalization capability, i.e., they can provide reliable prediction of the high-fidelity model response at the designs not used in the training process. These advantages are normally translated into better efficiency (in particular, lower CPU cost) when physics-based surrogates are used in the design optimization process (Koziel *et al.*, 2011).

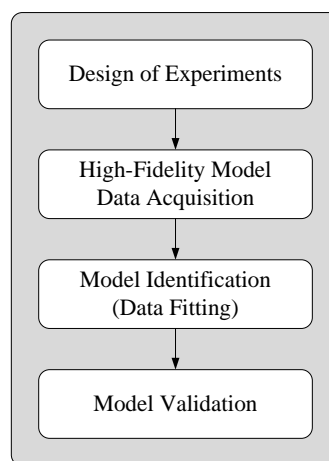


**Figure 3:** Data-driven surrogate model construction flowchart.

### 3.3 Data-Driven Surrogates via Kriging Interpolation

Kriging is a popular technique for interpolating deterministic noise-free data (Journal and Huijbregts, 1981; Simpson *et al.*, 2001; Kleijnen, 2009). In its basic formulation, kriging (Journal and Huijbregts, 1981; Simpson *et al.*, 2001) assumes that the function of interest is of the following form:

$$\mathbf{f}(\mathbf{x}) = \mathbf{g}(\mathbf{x})^T \boldsymbol{\beta} + Z(\mathbf{x}), \quad (1)$$

where  $\mathbf{g}(\mathbf{x}) = [g_1(\mathbf{x}) \ g_2(\mathbf{x}) \ \dots \ g_K(\mathbf{x})]^T$  are known (e.g., constant) functions,  $\boldsymbol{\beta} = [\beta_1 \ \beta_2 \ \dots \ \beta_K]^T$  are the unknown model parameters (hyperparameters), and  $Z(\mathbf{x})$  is a realization of a normally distributed Gaussian random process with zero mean and variance  $\sigma^2$ . The regression part  $\mathbf{g}(\mathbf{x})^T \boldsymbol{\beta}$  is a trend function for  $\mathbf{f}$ , and  $Z(\mathbf{x})$  takes into account localized variations. The covariance matrix of  $Z(\mathbf{x})$  is given as

$$\text{Cov}[Z(\mathbf{x}^{(i)})Z(\mathbf{x}^{(j)})] = \sigma^2 \mathbf{R}([R(\mathbf{x}^{(i)}, \mathbf{x}^{(j)})]), \quad (2)$$

where  $\mathbf{R}$  is a  $p \times p$  correlation matrix with  $R_{ij} = R(\mathbf{x}^{(i)}, \mathbf{x}^{(j)})$ . Here,  $R(\mathbf{x}^{(i)}, \mathbf{x}^{(j)})$  is the correlation function between sampled data points  $\mathbf{x}^{(i)}$  and  $\mathbf{x}^{(j)}$ . The most popular choice is the Gaussian correlation function

$$R(\mathbf{x}, \mathbf{y}) = \exp \left[ - \sum_{k=1}^n \theta_k |x_k - y_k|^2 \right], \quad (3)$$

where  $\theta_k$  are the unknown correlation parameters, and  $x_k$  and  $y_k$  are the  $k^{\text{th}}$  components of the vectors  $\mathbf{x}$  and  $\mathbf{y}$ , respectively. The kriging predictor (Simpson *et al.*, 2001; Journal and Huijbregts, 1981) is defined as

$$\mathbf{s}(\mathbf{x}) = \mathbf{g}(\mathbf{x})^T \boldsymbol{\beta} + \mathbf{r}^T(\mathbf{x}) \mathbf{R}^{-1}(\mathbf{F} - \mathbf{G}\boldsymbol{\beta}), \quad (4)$$

where  $\mathbf{r}(\mathbf{x}) = [R(\mathbf{x}, \mathbf{x}^{(1)}) \ \dots \ R(\mathbf{x}, \mathbf{x}^{(p)})]^T$ ,  $\mathbf{F} = [\mathbf{f}(\mathbf{x}^{(1)}) \ \mathbf{f}(\mathbf{x}^{(2)}) \ \dots \ \mathbf{f}(\mathbf{x}^{(p)})]^T$ , and  $\mathbf{G}$  is a  $p \times K$  matrix with  $G_{ij} = g_j(\mathbf{x}^{(i)})$ . The vector of model parameters  $\boldsymbol{\beta}$  can be computed as  $\boldsymbol{\beta} = (\mathbf{G}^T \mathbf{R}^{-1} \mathbf{G})^{-1} \mathbf{G}^T \mathbf{R}^{-1} \mathbf{F}$ . Model fitting is accomplished by maximum likelihood for  $\theta_k$  (Journal and Huijbregts, 1981).

### 3.4 Physics-Based Surrogates via Multi-Point Space Mapping

Let  $\mathbf{c}: X_c \rightarrow R^m$ ,  $X_c \subseteq R^n$  denote the response vector of a computationally cheap representation of the high-fidelity model  $\mathbf{f}$  evaluation of the system of interest. It is assumed that the base set  $X_B = \{\mathbf{x}^1, \mathbf{x}^2, \dots, \mathbf{x}^N\} \subset X_R$  is available such that the high-fidelity model response is known at all points  $\mathbf{x}^j$ ,  $j = 1, 2, \dots, N$ . In general, we do not assume any particular location of these base points. The goal is to enhance the low-fidelity model  $\mathbf{c}$  and create a space-mapping-surrogate model  $\mathbf{s}$  using auxiliary mappings with parameters determined so that  $\mathbf{s}$  matches the high-fidelity model as well as possible at all base points. Because the low-fidelity model is assumed to be physics-based (meaning that it describes the same physical phenomenon as the high-fidelity model but with a different level of fidelity), we hope that the resulting surrogate model will retain a good match with the high-fidelity model over the whole region of interest.

A standard space mapping model is defined as (Bandler *et al.*, 2004)

$$\mathbf{s}_{SM}(\mathbf{x}) = \bar{\mathbf{s}}_{SM}(\mathbf{x}, \mathbf{p}), \quad (5)$$

where the space mapping parameters  $\mathbf{p}$  are obtained using the parameter extraction process

$$\mathbf{p} = \arg \min_{\mathbf{r}} \sum_{k=1}^N \|\mathbf{f}(\mathbf{x}^k) - \mathbf{s}_{SM}(\mathbf{x}^k, \mathbf{r})\|, \quad (6)$$

while  $\bar{\mathbf{s}}$  is a generic space-mapping model, i.e., the low-fidelity model composed with some suitable mappings. A model often used in practice has the form (Bandler *et al.*, 2004; Koziel *et al.*, 2011)

$$\bar{\mathbf{s}}_{SM}(\mathbf{x}, \mathbf{p}) = \bar{\mathbf{s}}_{SM}(\mathbf{x}, \mathbf{A}, \mathbf{B}, \mathbf{c}, \mathbf{d}) = \mathbf{A} \cdot \mathbf{c}(\mathbf{B} \cdot \mathbf{x} + \mathbf{q}) + \mathbf{d}, \quad (7)$$

where  $\mathbf{A} = \text{diag}\{a_1, \dots, a_m\}$ ,  $\mathbf{B}$  is an  $n \times n$  matrix,  $\mathbf{q}$  is an  $n \times 1$  vector, and  $\mathbf{d}$  is an  $m \times 1$  vector.

The flexibility of the model represented by (5)-(7) can be enhanced in many ways, e.g., by exploiting so-called “pre-assigned” or “implicit” parameters. These parameters are fixed in the high-fidelity model but can be freely modified in the low-fidelity model in order to allow a better alignment between the high-fidelity model and the surrogate (Bandler *et al.*, 2004; Koziel *et al.*, 2011).

### 3.5 Mixed Modeling

A mixed model can be constructed by using a data-driven layer on top of the standard space mapping model (Koziel and Bandler, 2012). Define an enhanced space mapping surrogate model as (Koziel and Bandler, 2012)

$$\mathbf{s}(\mathbf{x}) = \mathbf{s}_{SM}(\mathbf{x}) + \tilde{\mathbf{s}}(\mathbf{x}), \quad (8)$$

where  $\mathbf{s}_{SM}$  is the standard space mapping surrogate model (in Section 3.4), and  $\tilde{\mathbf{s}}$  is a data-driven model (such as the kriging model in Section 3.3). This has certain advantages: (i) a relatively good modeling accuracy can be obtained with limited high-fidelity model data due the space mapping approach implemented with an underlying physics-based low-fidelity model, (ii) the resulting surrogate is computationally as cheap as the low-fidelity model because the data-driven layer typically exploits analytical formulas, and (iii) it is possible to take advantage of any amount of available high-fidelity model data, so that modeling accuracy can be as good as required provided that the base set is sufficiently “dense”.

## 4 Numerical Examples

In this section, we consider the proposed approaches on two examples: Case I shows the UT simulation responses within a metal component and utilizes space mapping to construct a surrogate, and Case II shows the responses of a UT simulations of a rectangular flaw within an aluminum block.

### 4.1 Case I: Basic Responses within a Metal Component

The space mapping surrogate modeling technique (described in Section 3.4) is applied to an example of UT simulations on metal components immersed in a water bath during the inspection process. Figure 4 shows the NDE setup of the ultrasonic testing. The metal component is submerged in water with the ultrasonic transducers at a distance (the water path distance) of 0.1 m from the solid (aluminum in this case). The transducer may be placed on an angle to detect a variety of flaws, but in this particular case the transducer points directly onto the solid surface, i.e., the transducer is perpendicular to the solid surface (which is flat in this case). The responses (shown in Fig. 5) indicate the maximum amplitude of the response to a Kirchhoff sphere flaw at each grid location. The ultrasonic testing simulator utilized in this work is capable of solving both the Asymptotic Green’s Function (Roberts, 2004) (the higher fidelity model) and the Gaussian-Hermite Series Expansion (Thompson and Gray, 1983) (the lower fidelity model). Both models are described in Section 2.

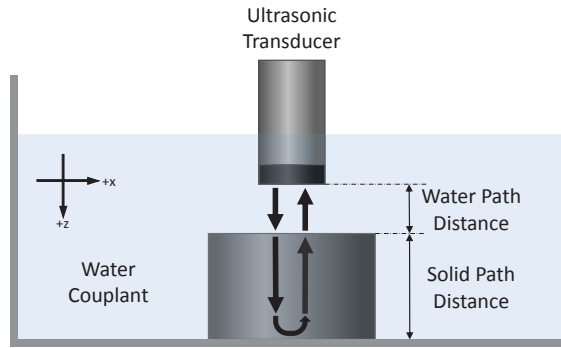


**Figure 4:** Setup for submerged ultrasonic nondestructive evaluation of metal components.

Responses of the UT simulations are given for the high- and low-fidelity models in Figs. 5(a) and 5(b), respectively. It can be observed that the responses by the two models have a similar shape, but the range of the voltage amplitudes are quite different. This gives an indication that the low-fidelity model follows the high-fidelity one, i.e., the models seem to be well correlated, at least for this given modeling situation. Having well correlated variable-fidelity models is key in physics-based surrogate modeling.

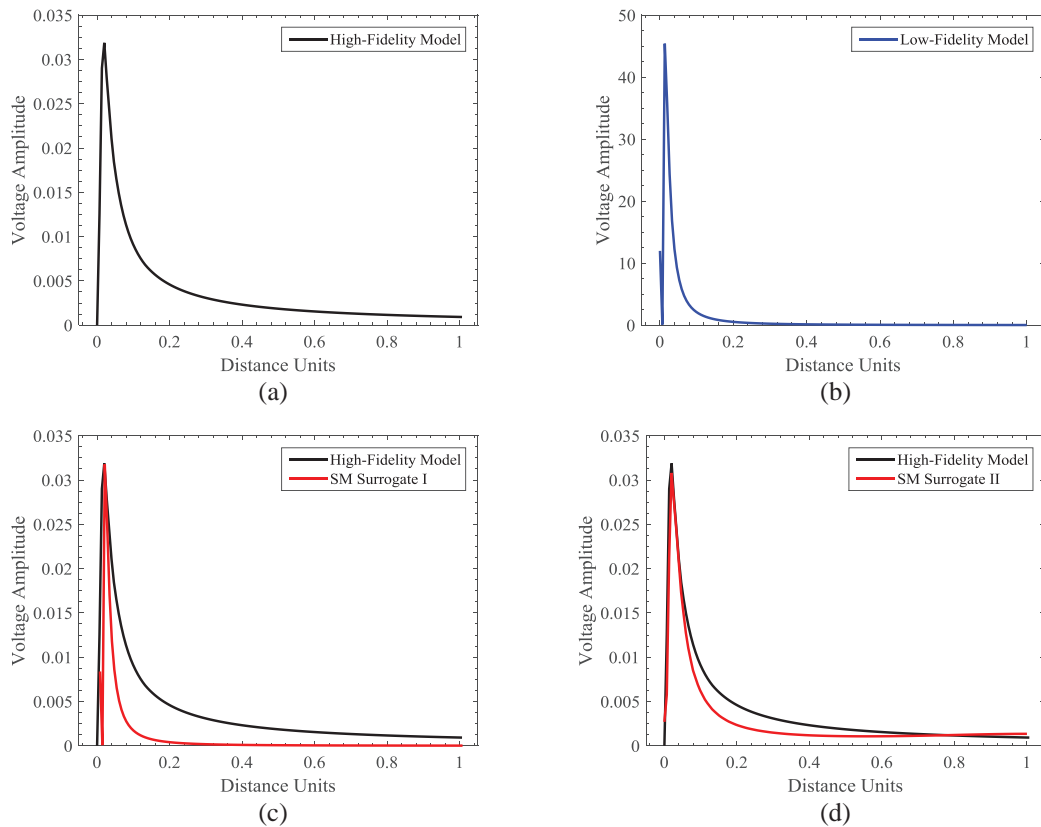


**Figure 5:** Ultrasonic testing simulation responses and space mapping (SM) surrogate model responses within the solid showing voltage amplitudes versus distance.



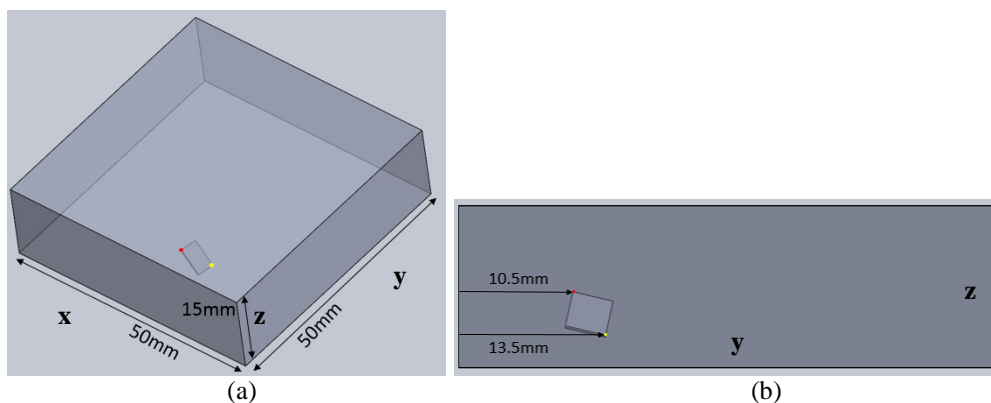
A space mapping surrogate (SM Surrogate I) is constructed by using two types of corrections, a multiplicative output correction and an input additive correction, applied to the low-fidelity model. Figure 5(c) shows a comparison of that surrogate with the high-fidelity model. These simple corrections align the peak amplitude and location of the peak of the high-fidelity model with the surrogate. However, the remainder of the surrogate response still needs further correction to match better with the high-fidelity model. Therefore, another space mapping surrogate (SM Surrogate II) is constructed using the first one, but adding a simple scaling of the distance axis. Figure 5(d) shows a comparison of that surrogate with the high-fidelity one and shows an improved alignment of the two models. Still, further model alignment is needed.

## 4.2 Case II: Responses of a Hypothetical Flaw within a Metal Block

In this case, we investigate the use of UTSim with a rectangular block of aluminum, shown in Fig. 6, and a rectangular flaw inserted at an arbitrary position and orientation. This mimics the nature of structural flaws, as the geometric properties are often unknown until further analysis. In this case, however, we will assume that the geometry of the flaw is known.

The test case is built on parameters similar to those in Case I. The area surrounding the flaw will be simulated to measure the flaw. To do this, we define a local grid around the flaw, where  $\Delta x$  and  $\Delta y$  are the change in position of the grid location and are 1mm each. A water path of 2.5mm is used, and an extra 2.5mm of space below the bottom surface is allowed to ensure there are no conflicts in computations, which therefore defines the  $z$  grid dimension to be 20mm. Each simulation uses a 1mm  $\times$  1mm grid in the  $xy$  plane, while varying the number of points in the  $z$  direction, denoted as  $n_z$ . This is the defining parameter in each of the variable fidelity models.  $n_z = 401$  in the high-fidelity model (f), and  $n_z = 21$  in the low-fidelity model (c). This results in each  $z$  grid being evaluated with  $\Delta z = 0.05$ mm and  $\Delta z = 1$ mm in f and c, respectively. Five sampling points were chosen, and each corresponds to either one of the four corners or the center of the flaw. Referring to Fig. 6, these are ordered clockwise starting at sample point 1, identified with the red dot. Sample point 3 is identified with the yellow dot, and sample point 5 is at the center of the flaw. Table 1 corresponds to the data obtained in Fig. 7 at each location.

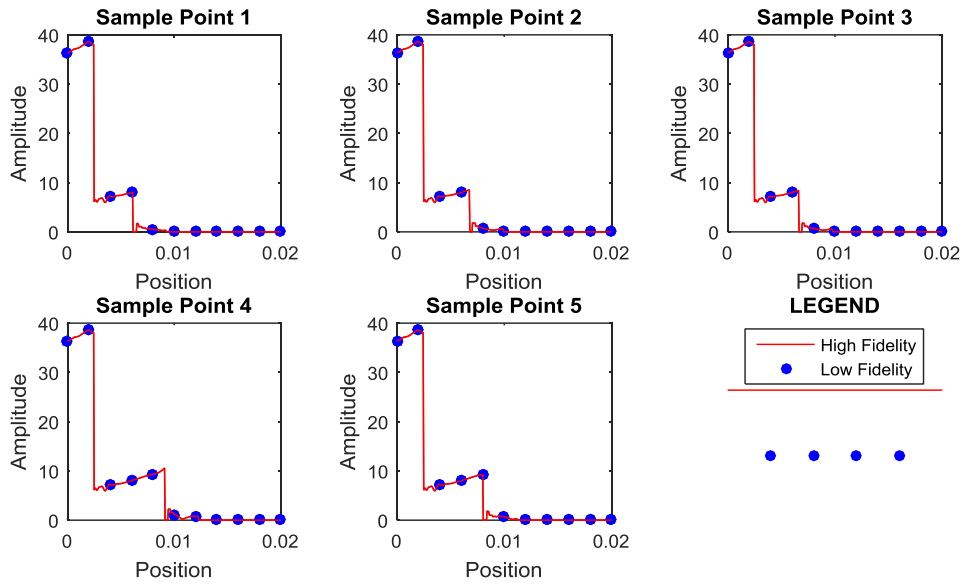
In each graph of Fig. 7, the first large drop represents the ultrasonic pulse propagating through water, then hitting the top of the aluminum test sample. The next large drop in amplitude is where the wave hits the flaw. The location of the flaw is determined to be the point at the bottom of this amplitude drop, since this marks the first incidence of notable change (after the water-solid interface). The points from c are overlaid on f, and this shows differences in where the flaw is located at each sampling point.



**Figure 6:** A hypothetical flaw placed in an aluminum box. The red and yellow dots are opposite corners on the top surface of the flaw used to define the flaw position.

**Table 1. Flaw depth locations.**

Sample Point	Depth (f)	Depth (c)	Error
1	6.15 mm	7 mm	13.8%
2	6.8 mm	7 mm	2.9%
3	8.05 mm	9 mm	11.8%
4	9.15 mm	10 mm	9.3%
5	6.65 mm	7 mm	5.3%

**Figure 7:** Amplitude plots of each sampling point.

We see that sampling points 1, 3, and 4 have errors of 9% or greater, or almost 1mm, and sampling point 2 has an error of less than 3%. Because **c** cannot determine the location of these flaws with consistent accuracy, the issue of reliability arises. When running large quantities of simulations, the difference in computation time becomes a very limiting factor when comparing thousands of sets of data, especially when fine models need to be used in order to characterize flaws with high accuracy. In future work, we investigate the development of a surrogate-based model to return accurate results for these simulations with low computational cost compared to fine models.

## 5 Conclusion

Having fast surrogate models for ultrasonic testing (UT) simulations is key for inverse analysis and model-assisted probability of detection (MAPOD) in the field of nondestructive evaluation. In fact, it is impractical to perform the aforementioned tasks in a timely manner using current simulation models directly. Fast surrogate models can make these processes computationally tractable. Several surrogate modeling techniques for UT simulations are proposed, and a combination of data-driven and physics-based surrogate models seem to offer a viable option. In future work, we will implement the proposed methods and apply them to inverse problems and MAPOD involving UT simulations.

## References

- Bandler, J.W., Cheng, Q.S., Dakroury, S.A., Mohamed, A.S., Bakr, M.H., Madsen, K., Søndergaard, J. (2004) "Space mapping: the state of the art," *IEEE Trans. Microwave Theory Tech.*, 52, pp. 337–361.
- Berens A.P. (1989) "NDE Reliability Data Analysis", ASM Metals Handbook, volume 17, 9th edition: Nondestructive Evaluation and Quality Control, ASM International, Materials Park, Ohio, pp. 1437-1470.
- Journal, A., and Huijbregts, C. (1981) "Neural network inverse modeling and applications to microwave filter design," *IEEE Transactions on Microwave Theory and Techniques*, 56:867-879.
- Kleijnen, J. (2009) "Kriging metamodeling in simulation: a review," *European Journal of Operational Research*, 192:707-716.
- Koziel, S., and Bandler, J. (2012) "Accurate modeling of microwave devices using kriging-corrected space mapping," *International Journal of Numerical Modelling*, 25:1-4.
- Koziel, S., Echeverría-Ciaurri, D., and Leifsson, L. (2011) "Surrogate-based methods," in S. Koziel and X.S. Yang (Eds.) *Computational Optimization, Methods and Algorithms*, Series: Studies in Computational Intelligence, Springer-Verlag, pp. 33-60.
- Meeker, W.Q. (2012) "R.B. Thompson's Contributions to Model Assisted Probability of Detection", AIP Conference Proceedings. Vol. 1430, pp. 83-94. doi: 10.1063/1.4716215
- MIL-HDBK-1823A (2009) Nondestructive Evaluation System Reliability Assessment, Available for download at <http://mh1823.com/mh1823>.
- Roberts, R. (2004) "Phased Array Beam Modeling Using a Discretely Orthogonal Gaussian Aperture Basis," *Proceedings Review of Progress in Quantitative Nondestructive Evaluation Vol. 23*, Thompson, D.O., and Chimenti, D.E., Eds., Plenum Press, N.Y., pp.785-792.
- Roberts, R., and Friedl, J. (2005) "Phased Array Inspection of Titanium Disk Forgings Targeting #1/2 FBH Sensitivity," *Proceedings Review of Progress in Quantitative Nondestructive Evaluation Vol. 24*, D.O. Thompson and D.E. Chimenti, Eds., AIP, N.Y., pp.922-929.
- Roberts, R., Thompson, R.B., Umbach, J., and Friedl, J. (2011) "Phased Array Transducer for Billet Inspection," *Proceedings Review of Progress in Quantitative Nondestructive Evaluation Vol. 30*, D.O. Thompson and D.E. Chimenti, Eds., AIP, N.Y., pp. 874-881.
- Simpson, T., Maurey, T., Korte, J., and Mistree, J. (2001) "Kriging models for global approximation in simulation-based multidisciplinary design optimization," *AIAA Journal*, 39:2233-2241.
- Smith, K., Thompson, R. B., Meeker, B., Gray, T., and Brasche, L. (2007) "Model-assisted probability of detection validation for immersion ultrasonic application", AIP Conference Proceedings, Vol. 894, pp. 1816-1822.
- Thompson, R.B., and Gray, T. (1983) "A model relating ultrasonic scattering measurements through liquid-solid interfaces to unbounded medium scattering amplitudes", *J. Acoust Soc. Am.* 74, pp. 1279-1290.
- Thompson, R.B. Meeker, W.Q., Brasche, L.J.H., Li, M., Klaassen, R., Umbach, J., Wasan, H., Hassan, W., Singh, S., Smith, K., and Patton, T. (2012) "Ultrasonic Probability of Detection Curves for Synthetic Hard Alpha Inclusions in Titanium Forgings", FAA Report No. DOT/FAA/AR-11/23.